



Relevance of Free Jet Model for Soil Erosion by Impinging Jets

Zeyd Benseghier, P. Cuéllar, Li-Hua Luu, J.Y. Delenne, Stéphane Bonelli, P. Philippe

► To cite this version:

Zeyd Benseghier, P. Cuéllar, Li-Hua Luu, J.Y. Delenne, Stéphane Bonelli, et al.. Relevance of Free Jet Model for Soil Erosion by Impinging Jets. *Journal of Hydraulic Engineering*, 2020, 146 (1), pp.04019047. 10.1061/(ASCE)HY.1943-7900.0001652 . hal-02609790

HAL Id: hal-02609790

<https://hal.inrae.fr/hal-02609790>

Submitted on 5 Sep 2023

HAL is a multi-disciplinary open access archive for the deposit and dissemination of scientific research documents, whether they are published or not. The documents may come from teaching and research institutions in France or abroad, or from public or private research centers.

L'archive ouverte pluridisciplinaire **HAL**, est destinée au dépôt et à la diffusion de documents scientifiques de niveau recherche, publiés ou non, émanant des établissements d'enseignement et de recherche français ou étrangers, des laboratoires publics ou privés.

Relevance of the free jet model for the soil erosion by impinging jets

Zeyd Benseghier¹, Pablo Cuéllar², Li-Hua Luu³, Jean-Yves Delenne⁴, Stéphane Bonelli⁵, and
Pierre Philippe⁶

¹PhD Student, IRSTEA, French Research Institute of Science and Technology for Environment
and Agriculture, 3275 route de Cézanne, 13100 Aix-en-Provence, France. E-mail:
zeyd.benseghier@irstea.fr

²Research supervisor, PhD, BAM, Federal Institute for Materials Research and Testing, Division
7.2 for Buildings and Structures, Unter den Eichen 78, 12205 Berlin, Germany. E-mail:
pablo.cuellar@bam.de

³Associate researcher, PhD, IRSTEA, French Research Institute of Science and Technology for
Environment and Agriculture, 3275 route de Cézanne, 13100 Aix-en-Provence, France. E-mail:
li-hua.luu@irstea.fr

⁴Director of research, PhD, INRA/CIRAD/Montpellier Supagro/UM2, 2 place Pierre Viala,
34060 Montpellier, France. E-mail: jean-yves.delenne@irstea.fr

⁵Director of research, PhD, IRSTEA, French Research Institute of Science and Technology for
Environment and Agriculture, 3275 route de Cézanne, 13100 Aix-en-Provence, France. E-mail:
stephane.bonelli@irstea.fr

⁶Director of research, PhD, IRSTEA, French Research Institute of Science and Technology for
Environment and Agriculture, 3275 route de Cézanne, 13100 Aix-en-Provence, France. E-mail:
pierre.philippe@irstea.fr

ABSTRACT

The surface erosion of soil samples caused by an impinging jet can be analyzed with the Jet
Erosion Test (JET), a standard experimental test to characterize the erosion resistance of soils. Here

we specifically address the flow characteristics of a laminar impinging jet over the irregular surface of granular beds to discuss the pertinence and relevance of commonly used empirical estimations based on the self-similar model of a free jet. The JET is here investigated at the micro-scale with a coupled fluid-particle flow numerical model featuring the Lattice Boltzmann Method (LBM) for the fluid phase combined with the Discrete Element Method (DEM) for the mechanical behavior of the solid particles.

We confront the hydrodynamics of a laminar plane free jet with the results from a parametric study of the jet impingement, both on solid smooth and fixed granular surfaces, which take into account variations of the particle size, of the distance from the jet origin, and of the jet Reynolds number. The flow characteristics at the bed surface are here quantified, including the maximal values in tangential velocity and wall shear stress, which can be regarded as the major cause for particle detachments under hydrodynamic solicitation.

We show that the maximal velocity at the impinged surface can be described by the free jet self-similar model, provided that a simple empirical coefficient is introduced. We further propose an expression for the maximal shear stress in laminar conditions including a Blasius-like friction coefficient that is inversely proportional to the square root of the jet Reynolds number.

To conclude, we finally analyze the JET erosion of different cohesionless granular samples, confirming that the threshold condition at the onset of granular motion is consistent with the Shields diagram and also in close agreement with previous experimental results.

Keywords: Free jet, Impingement jet, Lattice Boltzmann Method, Soil erosion, Laminar flow, Discrete Element Method.

INTRODUCTION

The impinging jet is widely encountered in numerous natural and industrial applications, such as heat transfer (heating, cooling and drying) (Martin 1977; Jambunathan et al. 1992), discharge of pollutants in rivers, lakes, and oceans (Gholamreza-Kashi et al. 2007), and headcut erosion (Bennett and Alonso 2005). The jet flow configuration has been profusely studied in the past both from theoretical and experimental perspectives (Beltaos and Rajaratnam 1973; Beltaos and

Rajaratnam 1974; Rajaratnam 1976; Hanson et al. 1990; Looney and Walsh 1984; Poreh et al. 1967; Ghaneeizad et al. 2015; Phares et al. 2000), often addressing the particular cases of the free jet and wall jet with a special focus on their self-similarity features.

Notably, the case of the impinging jet bears great interest in the field of civil engineering, where it is specifically used to quantify the resistance against erosion of cohesive soils. The erodibility of soils is a key parameter for the safety of earthen hydraulic structures such as earth-dams, levees, and dikes against the risk of erosion-induced failures (Foster et al. 2000; Bonelli 2012; Bonelli 2013).

The JET testing device (Jet Erosion Test) was firstly introduced by Hanson and Cook (2004) in order to assess the erosion rate E of soils for given flow conditions, with particular devices developed both for laboratory and *in situ* conditions. The interpretation of the test is based on the assumption that the rate of erosion is proportional to the excess of hydraulic shear stress τ exerted on the soil surface over a critical value τ_c at which the erosion will initiate. In mathematical form, this assumption reads $E = k_d(\tau - \tau_c)$, where the parameters τ_c and k_d are the critical shear stress and the erosion rate coefficient respectively, which define the soil's erodibility.

The rate of erosion is usually quantified by measuring the depth of the scour hole generated by the jet impingement on the soil surface over time. Then, the free jet theory can be applied to estimate the hydraulic shear stress on the soil surface, so that empirical values for the soil's erodibility (i.e. for τ_c and k_d) can be quantified by fitting the experimental data. It can be noted that such approach only considers the free jet theory (Schlichting 1960; Bickley 1937) and wall shear stress estimates on a smooth wall (Beltaos and Rajaratnam 1977; Beltaos and Rajaratnam 1974; Hanson et al. 1990) without taking into account the possible recirculation of the flow inside the scour crater nor any irregularity or roughness of the impinged surface.

A relevant weakness of this testing procedure is that the interpretation of the results is still based on strong assumptions for the estimation of the excess shear stress. Furthermore, the complex hydrodynamics of the impinging jet flow, which itself depends on many parameters (e.g. nozzle diameter, jet Reynolds number -nature of the flow-, inlet velocity profile) as well as the type

of the impinged surface, make the determination of the flow characteristics at the bed surface not an easy task, especially in the presence of a scour crater.

Moreover, the estimation of the shear stress disregards any confinement and wall effects in the JET device, as if the experiments were performed in unconfined conditions. In this respect, Ghaneeizad and co-workers have shown that the maximum shear stress under confined conditions can be 2.4 times higher than the value estimated in the original JET (Ghaneeizad et al. 2015). Nevertheless, the present study is here restricted to the unconfined condition that allows however a direct comparison to existing experimental data as explained hereafter. Phares and co-workers (2000) gave a theoretical prediction of the wall shear stress produced by an impinging jet over a flat surface for various jet configurations (axially-symmetric and two-dimensional jets, both for turbulent and laminar flows). They found that some of the theoretical results are not consistent with the measured wall shear stress reported by previous experimental investigations of impinging jets.

Recent experimental studies have investigated the erosion caused by an immersed impinging jet on a granular material, see e.g. the work of Badr et al. (2014) for turbulent and laminar planar impinging jets. They found that the flow characteristics can actually be estimated using the self-similar free jet model. Subsequently, Brunier-Coulin et al. (2017a) proposed an empirical expression to model the jet velocity inside the scoured crater of a cohesionless artificial granular material (refractive index matched glass beads) for a laminar round impinging jet.

On the other hand, the numerical models are nowadays gaining growing relevance for studying small to large-scale engineering applications. Some of the difficulties of the experimental tests can be overcome using customized numerical simulations, which can provide an insight into the local parameters of the flow that are hardly measurable in the experiments. Past numerical studies of the Jet Erosion Test have generally involved two main approaches. A first mono-phasic approach consists in solving directly the Navier-Stokes equations for the fluid flow. Several different turbulence models can be used for the axisymmetric jet condition. The water/soil interface is thereby considered as a Lagrangian boundary, which is updated using a suitable erosion law and an adaptive re-meshing technique (Mercier et al. 2014). The second possibility is to use a combined bi-phasic

approach, where the soil is modeled as a collection of discrete particles described by Newton's second law of motion (e.g. with the Discrete Element Method, or DEM) and the fluid flow is reproduced by a suitable computational fluid dynamics method (CFD), either solving the Navier-Stokes or the Boltzmann equations. Given that the pertinence and validity of the erosion law are the main concern here, the latter bi-phasic approach has several advantages for simulating Jet Erosion Test, since no erosion law needs to be assumed *a priori*. Among the studies that have been carried out using this approach, Kuang and co-workers (2013) presented a 3D CFD-DEM model of a turbulent round air jet impinging on a granular bed, focusing mainly on the crater formation induced by the air jet. Concerning the surface erosion of a cohesive soil, the Lattice Boltzmann Method (LBM) has been coupled with the DEM for a micro-mechanical simulation of the 2D laminar impinging jet in (Cuéllar et al. 2015; Cuéllar et al. 2017), which constitutes the basis for the present study with an extended model. Such combination of the LBM-DEM methods appears as a promising technique for simulating a wide range of geomechanical problems, including soil erosion (Cuéllar et al. 2017; Lominé et al. 2013), various porous flows (Han and Cundall 2013), the fluidization of soils (Cui et al. 2014; Ngoma et al. 2018), and immersed granular avalanches (Mutaruka et al. 2014) for instance.

The purpose of the present contribution is to provide a numerical insight into both the free and impinging laminar plane free jet on either smooth or granular surfaces, thereby complementing the previous experimental work of Badr et al. (2014) and Brunier-Coulin et al. (2017a). We place a particular focus here on quantifying the flow characteristics at the granular surface, namely the maximum shear stress τ_m and the maximum tangential fluid velocity V , and discuss their relation to the free plane jet model in laminar regime, as illustrated in Fig. 1. Finally, we also address here the onset of jet erosion of a cohesionless granular sample and provide an interpretation of the results in terms of a Shields diagram.

The remainder of this paper is organized as follows: Firstly, we describe the numerical methods employed for this study in Sec. 2. In Sec. 3, the laminar two-dimensional free jet theory is presented and the corresponding numerical setup is described, followed by a parametric study of the free

jet for various flow conditions. Afterwards, we analyze in detail the jet impingement on both a smooth wall and on a fixed granular surface. Sec. 4 finally deals with the full Jet Erosion Test on a cohesionless granular sample, discussing and comparing the numerical data with existing experimental and theoretical results from the literature. As a closure, Sec. 5 discusses the present findings and possible comparison with previous works before Sec. 6 provides a brief conclusion and outlines some open perspectives for future research.

NUMERICAL METHODS

Lattice Boltzmann Method

The LBM is used to simulate the fluid phase (jet flow) based on the solution of the discrete Boltzmann equation, as an alternative to other conventional CFD techniques that rely on the direct solution of the Navier-Stokes equations. It is usually solved in two main steps, namely a collision and a streaming step performed on an Eulerian spatial grid of nodes featuring a limited number of discrete velocity vectors for fluid particle populations. We use here the D2Q9 model (Qian et al. 1992), involving a two-dimensional space and nine velocity vectors \mathbf{c}_α defined in Eq. 3. For the collision model, we employ the multiple relaxation time approach (MRT) (Lallemand and Luo 2000) to overcome some well-known deficiencies (e.g. numerical stability issues) of the standard single relaxation time collision model of Bhatnagar-Gross-Krook (BGK) (Bhatnagar et al. 1954).

The multi-relaxation-time lattice Boltzmann equation can be written as:

$$f_\alpha(\mathbf{x} + \mathbf{c}_\alpha \Delta t, t + \Delta t) = f_\alpha(\mathbf{x}, t) - M^{-1} \mathbf{S} [m_\alpha(\mathbf{x}, t) - m_\alpha^{eq}(\mathbf{x}, t)] \quad (1)$$

where f_α are the discrete distribution functions (i.e. the probability density of fluid molecules with velocity \mathbf{c}_α in position \mathbf{x} and at time t) and \mathbf{S} is the diagonal relaxation matrix, $\mathbf{S} = \text{diag}(0, s_1, s_2, 0, s_4, 0, s_6, s_7, s_8)$. For the D2Q9 model, the coefficients $s_{1,2,4}$ are constants to be chosen in the range $0 < s < 2$ (for stability reasons) and $s_7 = s_8 = 1/\tau$, where τ is the relaxation

time related to the fluid kinematic viscosity as follows:

$$\nu = \frac{1}{3}(\tau - \frac{1}{2})\frac{(\Delta x)^2}{\Delta t} \quad (2)$$

We employ here the following relaxation rates after (Lallemand and Luo 2000): $s_1 = 1.63$; $s_2 = 1.14$; $s_4 = s_6 = 1.92$.

M is the invertible transformation matrix which links the distribution functions to their moment vectors m by $m = Mf$.

The macroscopic fluid variables for density ρ and velocity u can be obtained from the distribution functions as: $\rho = \sum_{\alpha=0}^8 f_{\alpha}$, $u = \frac{1}{\rho} \sum_{\alpha=0}^8 f_{\alpha} c_{\alpha}$.

The fluid pressure is directly given by the following state equation: $p = c_s^2 \rho$, where $c_s = c/\sqrt{3}$ is the speed of sound in the lattice system, $c = \Delta x/\Delta t$ is the characteristic lattice speed, Δx and Δt are the discretization units in space and time respectively.

It can be noted that we employ here the swap algorithm for the propagation step proposed in (Mattila et al. 2007; Latt 2007), which has the advantage of using and storing only one single copy of the density distribution functions f in memory. This algorithm requires the following special ordering:

$$c_{\alpha} \begin{cases} (0, 0) & \alpha = 0 \\ (-1, 1), (-1, 0), (-1, -1), (0, -1) & \alpha = 1, 2, 3, 4 \\ (1, -1), (1, 0), (1, 1), (0, 1) & \alpha = 5, 6, 7, 8 \end{cases} \quad (3)$$

It is also worth noting that the Lattice Boltzmann models can recover the incompressible Navier-Stokes equation through the Chapman-Enskog expansion (Chapman and Cowling 1970) when the density fluctuations are assumed to be negligible (Chen et al. 1992). Therefore, to correctly simulate an incompressible flow and reduce the density fluctuations of the model which lead to computational errors, the Mach number $Ma = |u_{max}|/c$ must be kept small as compared to unity: the maximum velocity in the system u_{max} should be much smaller than the sound speed c_s , usually with a limit value of $Ma < 0.1$ as found in the literature. For this reason, we maintained a constant

characteristic speed of $c = \Delta x / \Delta t = 10$ m/s in our simulations to keep the Mach number smaller than 0.1.

The magnitude of the time-step Δt can then be calculated based on the choice of fluid viscosity ν and spatial discretization parameter Δx from the known solid particles (see the section on LBM-DEM coupling later on), while the relaxation parameter τ can be derived based on Eq. (2).

Boundary conditions

In the LBM, neither pressure nor velocity boundary conditions can be directly imposed, since these variables derive from the particle distribution functions f_α . Therefore, the unknown distribution functions must be properly defined to retrieve the desired values of the hydrodynamic quantities at the boundary nodes. Pressure and velocity boundary conditions can, for instance, be set by using the method proposed by Zou and He (1997). However, the alternative regularized method proposed by Latt and Chopard (2008) has been used here for the sake of stability to impose the pressure or velocity boundary conditions for the inlet velocity, since this method was found to be more stable in all of our simulation cases.

Alternatively, we also use here for comparison another boundary condition in which all the particle populations are constructed by considering only the equilibrium part (the so-called equilibrium boundary). The equilibrium boundary is somehow less accurate than the regularized method (see e.g. Fig. 3 later on), but has the merit of being much easier to implement.

The nonslip boundary condition between the fluid and a stationary solid wall can be imposed through the so-called bounce-back scheme. We use here the half-way bounce-back model, which assumes that the wall is located right in the middle between solid and fluid nodes and has been shown to feature a second-order numerical accuracy (Zou and He 1997).

Wall shear stress

The hydrodynamic shear stress exerted by the fluid on the wall can generally be derived using the shear stress tensor τ_{xy} , which is given by the following expression for a two-dimensional incompressible flow: $\tau_{xy} = \rho\nu(\partial_x u_y + \partial_y u_x)$.

To calculate the wall shear stress, an extrapolation is needed in order to evaluate the velocity

gradient at the wall. For the case of a horizontal wall located at $y = 0$ and where $\partial_x u_y$ is assumed to be negligible, the wall shear stress will be $\tau_{xy,w} = \rho\nu \left. \frac{du_x}{dy} \right|_{y=0}$.

On the other hand, the shear stress tensor also can be obtained in the LBM out of the non-equilibrium part of the distribution functions as proposed by Mei et al. (2002):

$$\tau_{xy} = \left(1 - \frac{1}{2\tau}\right) \sum_{\alpha} f_{\alpha}^{neq}(\mathbf{x}, t) (c_{\alpha,x} c_{\alpha,y}) \quad (4)$$

where $f_{\alpha}^{neq} = f_{\alpha} - f_{\alpha}^{eq}$, and $c_{\alpha,x}$ and $c_{\alpha,y}$ are the x and y components of the velocity vector α respectively.

Since we assume here that the wall surface is not directly located on a fluid node, we extrapolate linearly the shear stress on the wall boundary so that $\tau_{xy,w} = \tau_{xy}^{y=1} + \Delta(\tau_{xy}^{y=1} - \tau_{xy}^{y=2})$, where $y = 1$ and $y = 2$ are the locations in lattice units of the two next neighboring fluid nodes along the normal direction with respect to the wall. Δ is thereby the relative distance from the fluid node to the wall. Since the half-way bounce-back scheme is used here, Δ is assumed to be equal to 0.5. According to Mei et al. (2002), the estimation of the shear stress using the non-equilibrium part of the distribution functions (Eq. 4) is more accurate than that by using the velocity gradient.

Discrete Element Method

The DEM originally proposed by Cundall and Strack (1979) is used here to describe both the interaction and motion of the solid particles as governed by Newton's equations. The total force acting on a given particle is the summation of the interaction forces with other particles plus the hydraulic forces. The interaction force exerted by grain j on grain i is $\mathbf{F}_{ij} = f_n \mathbf{n} + f_t \mathbf{t}$ and \mathbf{n} and \mathbf{t} represent the unit normal and tangential vectors along the line of particle centers.

The contact forces (normal and tangential), as well as the torque, arise only whenever two particles overlap. The normal contact force f_n can then be calculated based on a linear viscoelastic model:

$$f_n = -k_n \delta_n - \gamma_n v_n \quad (5)$$

where v_n is the relative velocity in the normal direction, k_n is the normal contact stiffness and γ_n is

the normal viscous damping.

The tangential contact force f_t can also be computed using a linear viscoelastic model as:

$$f_t = -k_t \delta_t - \gamma_t v_t \quad (6)$$

where k_t is the tangential contact stiffness, δ_t is the relative shear displacement during each contact, γ_t is the tangential viscous damping and v_t is the relative tangential velocity.

The tangential "shear" force is here limited by considering Coulomb's friction law:

$$|f_t| \leq \mu_s f_n \quad (7)$$

where μ_s is the friction coefficient.

The torque acting on the particle due to the contact frictional force is then given by

$$\mathbf{T}_i = -(\mathbf{r}_i \mathbf{n}) \times (f_t \mathbf{t}) \quad (8)$$

We add here a rolling resistance at the contact $\mathbf{T}_{roll} = -\frac{\mathbf{v}_r}{|\mathbf{v}_r|} \mu_r r_{eff} f_n$, with the rolling velocity $\mathbf{v}_r = \boldsymbol{\omega}_i - \boldsymbol{\omega}_j$ defined by the difference in the angular velocities $\boldsymbol{\omega}_i$ and $\boldsymbol{\omega}_j$ of grains i and j respectively. $r_{eff} = \frac{r_i r_j}{(r_i + r_j)}$ is thereby the effective radius and μ_r is the rolling coefficient.

In order to obtain a stable simulation and integrate correctly the equations of motion, the time step Δt_{DEM} must be chosen below a critical value Δt_{cr} which represents the oscillation duration of the spring-mass system used to model two contacting particles. Δt_{cr} is thus calculated taking into account the smallest mass in the granular system m_{min} and the normal stiffness k_n as $\Delta t_{cr} = 2\pi\sqrt{m_{min}/k_n}$. The DEM time-step is then usually adopted as $\Delta t_{DEM} = \lambda \Delta t_{cr}$ with a time-step factor λ chosen around 0.1.

The coefficient of normal viscous damping γ_n can be derived from the coefficient of restitution e (Ting and Corkum 1992).

Once all the external forces, including the contact and hydraulic forces, are computed at a time

t , an integration algorithm of the velocity-Verlet type can be used to compute the new kinematic variables of the grain at time $t + \Delta t$ (Swope et al. 1982).

Coupling of the LBM and DEM

The fluid-solid interaction is here introduced with the model proposed by Bouzidi et al. (2001), which assumes a non-slip bounce-back condition at the solid boundary nodes. This model is adapted to the curvature of the particle's boundary through a linear interpolation of the post-collision distribution functions. As a consequence of the particle's translation, some of the solid boundary nodes may convert to fluid nodes, so that the unknown distribution functions must be recovered. Several techniques to solve this issue can be found for instance in (Lallemand and Luo 2003), where the unknown distributions functions of the fresh fluid node are simply approximated using the equilibrium distribution functions (Mansouri et al. 2016).

The total force and torque exerted by the fluid on a given particle can then be calculated with the momentum-exchange algorithm (Ladd 1994) and be introduced into the DEM calculation after conversion to physical units. The buoyancy effect (i.e. the submerged weight) is also considered by reducing the gravitational acceleration with the factor $(1 - \rho_f/\rho_s)$.

To overcome the unphysical situation in 2D simulations where no fluid paths exist through a densely packed sample of disks, we introduce a reduced "hydraulic" radius r_h of the grains in the LBM domain while keeping the particle's real radius r in the DEM domain (Cui et al. 2012; Boutt et al. 2007). The ratio r_h/r is generally set to values around 0.8, as suggested in (Cui et al. 2012).

We adopt a fixed spatial resolution ratio $2r_{min}/\Delta x$ of 10 as recommended by Yu et al. (2003), where r_{min} is the radius of the smallest particle. This ratio therefore defines the lattice discretization parameter Δx for a given sample of solid particles.

Since the LBM and DEM often require different time-step sizes (the DEM time-step being usually smaller than the LBM time-step), an efficient coupling between both methods can be adopted by introducing sub-cycles for the DEM algorithm (Han et al. 2007). To this end we fix here an integer sub-cycle number $n_p = \Delta t_{LBM}/\Delta t_{DEM}$, ratio of the LBM and DEM time-steps respectively. In this study, n_p is chosen equal either to 1 or 2 by adjusting the DEM time-step factor

λ .

The presented LBM-DEM coupling technique has been implemented in our in-house code and thoroughly validated in several previous works, see for instance (Ngoma et al. 2018). In Sec. 3 we present a further validation of the LBM model with the well-known laminar free jet theory.

Jet configurations

The methods and techniques presented so far are now used to study various jet flow configurations, namely the free jet and the impinging jet on either a smooth wall (case a) or on a fixed granular surface (case b). These configurations are illustrated in Fig. 2. We impose a bounce-back boundary condition (Chen et al. 1996) for the solid walls (i.e. for the nozzle boundaries and the smooth impinged surface), while we assume a Zou/He outlet condition with zero pressure (Zou and He 1997) for the exterior boundaries. For the jet's nozzle (nozzle width b) we consider the velocity inlet condition with either the regularized or the equilibrium methods as introduced in Sec. 2 and featuring a Poiseuille velocity profile. The mean velocity of the Poiseuille injection is thereby $u_j = \frac{2}{3}U_0$ with U_0 being the maximal velocity of the inlet. In these conditions, the jet Reynolds number can be defined as $Re_j = u_j b / \nu$. We consider here relatively high values of ν to keep the flow within the laminar regime, allowing thereby a direct comparison with recent experimental data from (Badr et al. 2014; Brunier-Coulin et al. 2017a).

For the impingement case (a), the simulation procedure and conditions are the same as for the free jet except for the additional horizontal wall located at an axial distance H from the nozzle. For the study case (b), the smooth wall is replaced by a fixed granular surface at the same distance H . The granular surface is generated here with a particle size dispersity of $d_{max}/d_{min} = 1.5$. Note that the DEM and the coupling technique with LBM is only active in this configuration.

The input values adopted for the parametric study are summarized in Tables 1 and 2 for the free jet and impinging jets respectively.

NUMERICAL RESULTS

Two-dimensional free jet

Multiple simulations were performed for various free jet conditions, with Reynolds numbers Re_j in the range of $19 < Re_j < 130$. Fig. 3 shows the numerical results as compared to the analytical solution of the centerline velocity with two different virtual origin adjustments (see the appendix I, which briefly summarizes the theoretical background for a 2D self-similar free jet in laminar regime). Note that, according to Eq. (18), the analytical solution does not originate from the maximal velocity at the nozzle exit. The slight departure from the analytical solution appears a bit more severe for the case with the equilibrium method inlet than for the regularized one. Nevertheless, the overall good agreement with the theory seems evident. The transversal profiles of fluid velocity depicted in Fig. 4a show that the velocity decreases continuously from its maximum value u_m at the centerline with growing lateral distance y . A normalized plot of the variables in Fig. 4b confirms that the velocity profiles are closely self-similar and well described by the theoretical prediction $[ch^{-2}(y/\tilde{b}_u)]$ for all horizons farther than $x > 1.5b$, i.e. beyond the point where the free jet exits the potential core region. This region normally extends up to around $6b$ for turbulent flows according to the literature (Hanson and Cook 2004; Beltaos and Rajaratnam 1977), and so it appears significantly reduced for the laminar conditions considered here. The normalization of the transversal coordinate y is here done employing the half-width b_u , which is the transversal distance where $u(b_u) = \frac{1}{2}u_m$ applies.

Fig. 5a shows the variation of $(u_j/u_m)^3$ and $(b_u/b)^{3/2}$ with the normalized distance x/b from the nozzle for a jet Reynolds number equal to $Re_j = 38.9$. The profiles are linear with slopes α and β , and negative x -intercepts denoted $-\lambda_u/b$ and $-\lambda_b/b$, respectively. The proportionality between u_m and $x^{-1/3}$, as well as between b_u and $x^{2/3}$, predicted by the theory (see Eqs. 18 and 19 in the appendix) appears here clearly confirmed. A further implication, stemming from the fact that the x -intercepts are different from zero, is that the origin of the jet is not located right at the nozzle exit, but at a virtual point source at a distance λ from it. Here, by convention, λ is positive when the virtual origin is above the nozzle exit.

Fig. 5b shows the variation of the slopes α and β with the jet Reynolds number in a log-log plot.

Here, the slope of the curve α versus Re_j is -1.107 , while its theoretical value is -1 (see Appendix I). This difference is not surprising in view of the slight departure in the centerline velocities u_m between the simulated and analytical results (see Fig. 3). Nevertheless, the proportionality $\alpha \propto Re_j^{-1}$ implied by Eq. (18) is here verified for almost the whole range $37 < Re_j < 120$. In the same vein, the proportionality $\beta \propto Re_j^{-1}$ derived from Eq. (19) also appears to be well verified here.

Concerning the virtual origin λ , the dimensionless quantity λ/b can be easily obtained from the x -intercept of any of the two linear profiles $(u_j/u_m)^3$ or $(b_u/b)^{3/2}$ versus x/b (i.e. from either A or B in Fig. 5a). The two different estimations of λ/b seem here to agree fairly (Fig. 6), with a mean relative error of 13%, and can be fitted with a linear trend that appears slightly higher than the existing solution $\tilde{\lambda}/b = 0.029Re_j$ given in (Revuelta et al. 2002). The trendline of the numerical data reads here:

$$\lambda = 0.036Re_j b \quad (9)$$

Impinging jets

Regarding now the impinging jet situation, the three main regions of fluid flow depicted in Fig. 2 can generally be distinguished (see e.g. (Beltaos and Rajaratnam 1973)): a free jet region (zone 1) in which the flow remains self-similar, an impingement region (zone 2) in which the impinged surface affects the jet flow, decreasing the centreline velocity down to zero at the impingement (stagnation) point and diverting the flow to the lateral directions, and finally a wall jet region (zone 3), where the flow becomes parallel to the impinged surface.

Many studies have addressed in detail the velocity, pressure, and shear stress fields for these regions, e.g. (Rajaratnam 1976; Ghaneeizad et al. 2015). However, the analysis of jet impingements in the frame of soil erosion still remains largely empirical. No simple analytical approach has been proposed so far for the prediction of the flow quantities at either the impingement region or at the wall jet region (zones 2 and 3 respectively). In this respect, most of the estimations in the literature are based on the free jet model (zone 1). This section therefore examines the influence of both the jet Reynolds number and impingement height H on the distributions of fluid velocity and shear

stress at the impinged surfaces. Thereby, we explore firstly the relationship between the free-jet centerline velocity at the impingement height $\tilde{u}_m(H)$ and the maximal velocity V of the impinging jet near the wall surface in zone 3, turning afterwards the attention to the maximal shear stress τ_m .

In the simulations presented here, we observed transverse oscillations of the jet when impinging a granular surface. These oscillations were only hardly noticeable for small values of Re_j and tended to intensify progressively with an increasing inlet velocity. Therefore and for the sake of consistency, here we analyzed the velocity field only at the moments where the jet is exactly vertical. In contrast, such jet oscillations were never observed in the simulations with a smooth wall.

Velocity field

Figs. 7a and 7b show the profiles of transverse velocity v at different distances x_1 from the impinged surface for the study cases (a) and (b) respectively. Note that the reference position $x_1 = 0$ for the fixed granular surface corresponds to the top of the uppermost particle. All profiles show a monotonic increase of velocity up to a maximum value v_m and a subsequent continuous decrease with growing distance y/H from the jet's axis. The local maximum of transverse velocity v_m of each profile increases rapidly with x_1 until reaching a global maximum $V = \max(v_m)$ and then decays slowly.

The global maximum of fluid velocity V over the impinged surface can be extracted for different flow conditions and samples (different mean grain sizes), and then be plotted versus the free-jet maximum velocity $\tilde{u}_m(H + \lambda)$ at the corresponding distance from the nozzle (Eq. 18), as shown in Fig. 8 in direct comparison to the smooth-wall results. We appreciate a close agreement of the data for the low velocity range, with growing deviations for higher fluid velocities and higher particle size due to the irregular form of the bed surface. We also notice that the trend is almost linearly proportional with a slope equal to 0.82 [case (a)], consistently for any given jet Reynolds number Re_j and distance H within the range of our simulation sets. Thereby, we replace H by $H + \lambda$ in order to take into account the virtual origin discussed previously (i.e. $\lambda/b = 0.036Re_j$), although the effect of λ on the slope appears to be negligible. These results therefore confirm that, for the case of a smooth surface, the maximum impingement velocity can indeed be estimated by means

of the free jet theory. Concerning the impingement on a granular surface, it appears sensible to approximate the maximum velocity just as for the smooth wall case at least for situations with low Reynolds numbers.

In the case of granular surfaces, the sensitivity to the impact point location was also tested for the same inlet flow condition as presented in Fig. 7b. To this end, several calculations were performed after a slight lateral displacement of the nozzle (up to 3 times the minimal diameter) in either direction. In all cases, the maximal velocity V was found consistent to a mean value within a reasonable error bar estimated to less than 5% from the standard deviation values. The same relative error is used for the other inlet flow conditions.

Wall shear stress

The simulated distribution of dimensionless wall shear stress is plotted in Fig. 9a for different combinations of impingement height H/b and jet Reynolds number Re_j . Despite the difference in the flow configuration (2D laminar versus round turbulent jet), the dimensionless shear stress distribution agrees quite well with that given by Beltaos and Rajaratnam (1974). Here, it can also be noted that the maxima of shear stress are actually located closer to the jet's axis than the corresponding maxima of fluid velocity (see Fig. 7)

The maximal value of τ is often assumed to be proportional to the square of the maximal velocity V (Beltaos and Rajaratnam 1977), namely in the form of $\tau_m = \frac{1}{2}C_f\rho V^2$, where C_f is the local friction coefficient and ρ is the fluid density.

The authors are not aware of any estimation of C_f for laminar impinging jets to be found in the literature. The typical value of C_f for turbulent flow conditions ranges around 4×10^{-3} , see e.g. (Beltaos and Rajaratnam 1974; Hanson and Cook 2004; Beltaos and Rajaratnam 1977). Based on the definition of τ_m , now we can use our simulation results to estimate C_f for the different jet Reynolds numbers and impingement heights H shown in Table 2.

A plot of the maximum shear stress τ_m versus $\rho V^2 / \sqrt{Re_j}$ is shown in Fig. 9b, suggesting a

linear dependency that permits to estimate C_f as:

$$C_f = \frac{1.53}{\sqrt{Re_j}} \quad (10)$$

This way, τ_m can be rewritten into:

$$\tau_m = \frac{0.765\rho V^2}{\sqrt{Re_j}} = \frac{0.52\rho(\tilde{u}_m(H + \lambda))^2}{\sqrt{Re_j}} \quad (11)$$

By introducing Eqs. (18) and (9), it then reads as:

$$\tau_m = \frac{0.137\rho u_j^2 Re_j^{1/6}}{(H/b + 0.036 Re_j)^{2/3}}. \quad (12)$$

Surprisingly, we found that the simulation results give close results compared to the estimation based on the Blasius friction law for a laminar boundary layer over a flat plate: $\bar{C}_f = 1.328/\sqrt{Re}$ (Streeter and Wylie 1975), where \bar{C}_f is the average friction coefficient over a plate of length L and $Re = U_\infty L/\nu$. Consistently with the development of a boundary layer, a scaling with $Re_j^{1/2}$ can be reasonably obtained for the x_1 -value of location of the maximal velocity. Similar results were also presented in (Phares et al. 2000) implying that the maximal shear stress within a laminar boundary layer scales with $Re_j^{-1/2} (H/b)^{-5/4}$ at $y/H = 0.12$ for fully developed 2D jet impingements ($H/b > 8$).

Summing up, these results show that the local friction coefficient at the maximum shear stress seems to be proportional to $1/\sqrt{Re_j}$ for laminar jets impinging on a smooth wall, just as predicted by the laminar boundary layer theory on flat plates at zero incidence. The maximum shear stress over a smooth wall can therefore be estimated using the approximation in Eq. (12) based on our simulation results.

Concerning the wall shear stress distribution at the granular surface, the strong fluctuations of shear stress related to the irregularity of the impinged surface generally preclude the appearance of smooth distributions such as the one shown in Fig. 9a. Nevertheless, and in absence of more specific estimations, it appears sensible to derive the wall shear stress over granular surfaces using

the previous approximation based on the maximum velocity V that was found for the smooth-wall case (Eq. 11).

ONSET OF EROSION FOR FRICTIONAL SAMPLES

We now turn the attention to the jet erosion, i.e. to the detachment of solid particles under the action of an impinging jet, for the case of a cohesionless granular bed. In this section, the solid particles are now let free to move based on purely frictional interactions (no cohesion) and under the hydrodynamic solicitations imposed by the impinging jet.

In general, the onset of erosion for cohesionless sediments can be described by the Shields number, which quantifies the erosion threshold as the ratio between the critical bed shear stress $\tau_s = \rho u_*^2$ and the submerged gravitational stress acting on the solid particles $(\rho_g - \rho)gd$, where d is the particle diameter while ρ_g and ρ are the grain and fluid densities respectively (Shields 1936). The abundant literature on the Shields diagrams shows that the erosion threshold can be well described by a critical Shields number Sh_τ^* solely dependent on the particle Reynolds number $Re_\tau^* = u_* d / \nu$, that is:

$$Sh_\tau^* = \frac{\tau_s}{(\rho_g - \rho)gd} = f(Re_\tau^*) \quad (13)$$

where u_* is the so-called friction velocity, or shear velocity, at the bed surface, and τ_s may be here approximated for a 2D laminar impinging jet from Eq. (11), or equivalently Eq. (12), as shown in the previous section.

Erosion threshold

In order to estimate the erosion threshold for a given cohesionless granular sample in our micromechanical JET simulations, we now let the particles move freely as we increase progressively the maximal inlet velocity U_0 over time until reaching a fully developed erosive state, as shown in Fig. 10. Then, we identify the critical inlet velocity U_0^c based on the observation of the first grain motion.

We repeated this procedure for various jet Reynolds numbers and three different samples

($d_{mean}=2, 3, \text{ and } 5 \text{ mm}$ respectively, featuring a uniform size distribution ranging from $d_{min} = 0.8d_{mean}$ to $d_{max} = 1.2d_{mean}$), thus providing a range of conditions to be displayed in the Shields diagram. The input data for this parametric study is summarized in Table 3.

We observe that the first granular motion generally takes place at a certain distance from the impingement (stagnation) point and corresponding roughly with the location of the maximal shear stress predicted in our analysis of the impinging jet over a smooth wall [see Fig. 9a]. However, by increasing progressively the inlet velocity, we observe at some point the appearance of lateral oscillations of the fluid jet caused by the irregularities of the bed surface, which in turn enhance the on-going scouring process. Due to the oscillations of the jet and the increasing depth of the crater, the location of the active erosion zone appears then to shift progressively towards the impingement point, thereby creating a deeper crater right under the jet's axis (see the graphical sequence shown in Fig. 10).

Shields diagram

The Shields diagram represents the relationship between the critical Shields number and the particle Reynolds number, estimated from the friction velocity, as obtained for various particles sizes and shapes in a wide range of flow conditions. Although the original Shields diagram presents solely scatter data, several empirical approximations have been subsequently proposed to fit the data. The explicit formulation of the Shields curve proposed by (Guo 1997; Guo 2002) reads for instance:

$$Sh_{\tau}^* = \frac{0.11}{Re_{\tau}^*} + 0.054 \left[1 - \exp \left(-\frac{4Re_{\tau}^{*0.52}}{25} \right) \right] \quad (14)$$

where Re_{τ}^* is the particle Reynolds number as defined before.

Here it is worth noting that this expression is sometimes inconvenient for a practical use (especially in complex flow configurations such as the impinging jet), since the shear velocity actually appears in both x and y variables of the Shields diagram (see Eq. 13). However, this can be circumvented with the alternative approach proposed by Badr et al. (2014) and later adopted by Brunier-Coulin et al. (2017a), representing an equivalent form of the Shields number for the

impinging jet. The idea is to assume an inertial expression Sh_u for the Shields number, considering that the shear stress is simply equal to ρu^2 , regardless of the flow regime. Here, following Badr et al. (2014), the velocity u is chosen as a characteristic fluid velocity around the eroded particle and can be directly estimated with the free jet model $\tilde{u}_m(H)$ instead of the shear velocity u_* at the impinged surface.

As a first test, we can compare quantitatively our simulation results to the experimental data of Badr et al. (2014), since their quasi-2D configuration is closely consistent with the two-dimensional conditions of our model. The equivalent Shields diagram proposed by Badr et al. (2014) relates the critical value of the inertial Shields number, Sh_u^* , to the critical particle Reynolds number $Re_p^* = \frac{ud}{\nu}$ as follows:

$$Sh_u^* = \frac{\rho[\tilde{u}_m(H)]^2}{(\rho_g - \rho)gd} = f(Re_p^*) \quad (15)$$

Sh_u^* is here evaluated from the expression of $\tilde{u}_m(H)$ given in Eq. (18), where u_j is given by the critical inlet velocity obtained for each simulation at the onset of erosion, $u_j = 2/3U_0^c$.

Here it is also important to note that, for a quantitative comparison, the expression of the inertial Shields number Sh_u has to be modified for the simulated results to account for the dimensional discrepancy of the solid particles, i.e. for the simulated disks in a plane instead of the solid spheres in the quasi-2D experimental configuration. The correction employed here is explained as follows. Firstly, we assume that the ratio of hydrodynamic drag force to the buoyant weight of a given particle is the same both for disks and spheres. This ratio reads $\frac{\tau_f S}{\Delta \rho g V} = Sh \frac{Sd}{V}$ where S and V are the cross-section and volume of the particle respectively. For disks or cylindrical particles, this expression leads to $\frac{Sd}{V} = \frac{4}{\pi}$, while for the case of a sphere $\frac{Sd}{V} = \frac{3}{2}$ is obtained. As a consequence, the inertial Shields number from the simulations is multiplied by $\frac{3\pi}{8}$ to be quantitatively comparable to the experimental data. Moreover, the reduced (hydraulic) diameter $d_h = 0.8d$ is also taken into account, as explained above.

Fig. 11 shows that a fair agreement of simulated and empirical data can be achieved this way. Our numerical values of Sh_u^* are in the range 1.16 ± 0.33 , comparing well with the results of Badr et al. (2014) which appear to show an almost constant value of $Sh_u^* = 1.2 \pm 0.6$ for a range of Re_p^*

from laminar to turbulent flows. In this respect, our numerical data rather suggest a slight decrease of Sh_u^* with Re_p^* .

Not only the inertial Shields number Sh_u but also the usual Shields number defined by the real fluid shear stress, Sh_τ , can be calculated out of the numerical results based on Eq. (12). This way, the previous results can be plotted in the classical Shields diagram through Eq. (13). This can also be done for the experimental data of Badr et al. (2014) if we assume the same friction coefficient C_f as given in Eq. (10) from our LBM calculations with laminar impinging jets. The corresponding values of the critical Shields numbers Sh_τ^* for both experimental and numerical results as compared to the explicit formulation in Eq. (14) are shown in Fig. 12 as a function of the particle boundary Reynolds number Re_τ^* .

Here the quantitative agreement between the present numerical results and the experimental data by Badr et al. (2014) is slightly worse than by using the inertial Shields number Sh_u^* . Nevertheless, both data sets appear relatively close to the explicit Shields curve, with the simulated data laying slightly above it and the experimental one slightly below. Furthermore, a slight decrease of Sh_τ^* with Re_τ^* can now be observed more clearly for this range of particle Reynolds number Re_τ^* , generally consistent with the trend shown by the Shields curve.

DISCUSSION

The main results of the present study can be summarized as follows. Firstly, the results obtained with our LBM model of a 2D jet flow show high accuracy when compared to the laminar self-similar solution of a plane free jet for jet Reynolds numbers up to almost 130, thus extending previous comparisons with experimental data which were limited to jet Reynolds numbers under 30 (Phares et al. 2000; Looney and Walsh 1984; Andrade 1939). Regarding the jet impingement on a smooth wall, our findings also confirm that a laminar boundary layer develops at the wall departing from the stagnation point and featuring a friction coefficient that scales with $Re_j^{-1/2}$, as already shown by Phares et al. (2000). On this basis, we propose here an accurate expression for the maximal bed shear-stress. On the other hand, and despite a greater scatter of the results, the data obtained for the impingement on a fixed granular wall appears broadly consistent with the

previous simulations on a smooth wall with respect to the maximal velocity reached by the flow in the impingement zone. To conclude, we finally propose a direct confrontation of our numerical results for granular erosion with the experimental data for three-dimensional planar jet erosion obtained by Badr and co-workers (2014). We find that the good quantitative agreement with the experimental data endorses the further use of our LBM-DEM modelling approach and appears to support our novel estimation of maximal shear-stress for the Shields diagram.

However, for several reasons the outcomes proposed within this study cannot be directly compared to real flow conditions, which are usually highly turbulent both in the context of soil erosion and particularly in complex applications such as the Jet erosion test.

To begin with, our LBM model is not yet adapted to natural turbulent water flows and therefore it was used here to simulate only laminar jets. Nevertheless, and beyond the fact that the flow impinging a granular bed is often laminar at the upper jet inlet, the redirection of the flow and the interaction with the sediment bed through intermittent and localized flow structures allow to explore not only the laminar flow domain but also the transitional one regarding the Shields diagram (i.e. Re_τ up to about 20 in Fig. 12). Indeed, our results compare reasonably well with the experimental data by Badr and co-workers that was produced not only with laminar jets but also with turbulent jets, with jet Reynolds numbers up to around 1000 (Badr et al. 2014). On the other hand, in this respect it also appears important to note that the alternative use of a mean fully-turbulent modeling approach, possibly added to the LBM by means of a LES scheme (Large Eddy Simulation) as proposed in Feng et al. (2007), would probably not be able to reproduce the unsteady and short-lived flow bursts that can be observed in the simulations with our current model.

A second reason that prevents our findings from being directly applicable for a real JET test, whether in the lab or in the field, is the limitation of our models to 2D and plane jet conditions, whereas the jets that are commonly used in practice are naturally three-dimensional and round. Consequently, only qualitative comparisons can be expected between the 3D circular and the 2D planar impinging jets, particularly since the respective analytical free jet solutions show different scaling laws due to the increased lateral dispersion in 3D (Bickley 1937; Schlichting 1960).

The applicability of the present models would certainly increase substantially if both the 3D as well as the turbulent flow conditions were implemented in our algorithms. However, such an improvement would also involve a considerable increase of both the computational cost and necessary resources in terms of processing power and storage that at present we only envisage as a future objective. In this sense, the models presented here can therefore be considered as a first step on this route, but already with the major advantage of allowing a direct comparison with experimental data, which is relatively scarce in relation to jet erosion.

And finally, further discussion can also be focused on the way to compare quantitatively the impinging planar jets and their related erosion onset between the 2D conditions in the present numerical study and the 3D reality in the experiments by Badr et al. (2014). In this respect we may first note that several aspects of the experimental conditions were different from their numerical counterparts: in the experiments, the grains were significantly smaller in size, from 0.1 to 1mm, while the liquid used for the jet flow was either water or glycerol-water mixtures with a viscosity not greater than four times that of water. By contrast, the numerical simulations featured larger particles (with 2, 3 and 5 mm in mean grain size) and much more viscous fluids (30 to 50 times the water viscosity). Nevertheless, we show here that these differences do not prevent a quantitative comparison assuming the relevance of the Shields diagram approach based on dimensionless numbers, namely the Shields number and the particle Reynolds number, which cover approximately the same ranges. Therefore, the main issue here rather comes from the natural differences in terms of geometry: an assembly of disks with a 2D impinging flow versus a bed of spherical particles impinged by a 3D planar jet. As explained beforehand, the expression of the Shields number in 2D with disks can be modified based on the mechanical equilibrium at the particle scale. This feature leads to an accurate agreement with the experimental data when using the inertial Shields numbers as shown in Fig. 11. In contrast, the agreement appears less convincing when the correct dimensionless numbers needed in the Shields approach are used. However, this latter approach seems questionable since it is based on several major simplifications. For instance, the fluid friction coefficient in Eq. (10) is probably slightly different between the 2D jet and the 3D

planar jet. Furthermore, the relationship between the hydrodynamic drag force and the bed shear-stress may also be different between a sphere and a disk (or a cylinder), including the potential influence of the numerical hydraulic diameter. And finally, the effective maximal shear-stress exerted on the sediment bed is probably different from the one calculated on a smooth wall. All in all, it appears that our crude estimate of Shields number in 2D is probably compatible with the factor of about 2 that, according to Fig. 12, could account for the almost systematic discrepancy between the Shields curve and our numerical results.

CONCLUSIONS AND OUTLOOK

Some 2D laminar flow configurations of both free jet and impinging jet on a horizontal surface have been investigated here using the numerical Lattice Boltzmann Method (LBM). We show that the flow simulations are accurate for various jet Reynolds numbers by introducing the virtual origin λ , as validated with the self-similarity theory of the free jet.

The simulations of the impinging jet for both a smooth wall and a fixed granular surface have further shown that the maximal tangential velocity in the vicinity of the surface is directly proportional to the free-jet velocity at a corresponding downstream distance as computed with the self-similar theory. The results therefore confirm that the free-jet velocity $\tilde{u}_m(H)$ can be used as the characteristic impingement velocity when the virtual origin is taken into account. Furthermore, we have proposed here an expression for the maximal shear stress at the surface (Eq. 11) based as well on the free-jet theoretical velocity and including an additional friction coefficient of the Blasius type that is inversely proportional to the square root of the jet Reynolds number.

Finally, we have addressed the onset of jet erosion for frictional (cohesionless) granular samples by means of two-dimensional simulations of the Jet Erosion Test (JET) with a coupled LBM-DEM technique. The simulated results appear in fair agreement with the experimental data of Badr et al. (2014) for plane impinging jets regarding two different definitions of the Shields number, namely the inertial expression Sh_u^* and the usual one Sh_τ^* . The classical Shields diagram was well reproduced in the latter case.

As a perspective, we are currently extending our JET simulations to the case of cohesive granular

618 samples with varying particle sizes and inter-particle cohesion, aiming to verify the generalization
619 of the Shields number for cohesive granular materials proposed by Brunier-Coulin et al. (2017b).

620 **DATA AVAILABILITY**

621 All data generated during the study are available from the corresponding author by request
622 while the code used remains proprietary.

623 **ACKNOWLEDGMENTS**

624 Z. Benseghier is grateful for the financial support provided by the "Région Sud, Provence-
625 Alpes-Côte d'Azur" and the valuable exchanges with D. Chausseé (Suez Consulting Corp.). The
626 authors would also like to thank F. Lominé, J. Duriez and J. Ngoma for fruitful discussions.

APPENDIX I. TWO-DIMENSIONAL FREE JET

The two-dimensional free jet has been studied in the past by many researchers. Schlichting (1960) provided a solution describing a round jet based on the boundary-layer approximation, while Bickley (1937) gave an analytical solution for the two-dimensional case. The latter is based on the assumption that the momentum flux M remains constant so that the free jet flow remains self-similar with the downstream distance x from a source point. For the remainder, we introduce the index (\sim) to denote the analytical variables and distinguish them from the simulated ones.

The self-similarity of a plane free jet implies that the longitudinal velocity of the fluid at any point downstream of the nozzle can be described by:

$$\tilde{u}(x, y) = \tilde{u}_m(x)f(\eta) \quad (16)$$

where \tilde{u}_m is the fluid velocity along the jet axis (i.e. the maximal velocity at the horizon x) and f is the similarity function in the following form: $f(\eta) = 1/\text{ch}^2(\eta)$ with $\eta = y/\tilde{\Delta}(x)$. Here, η is the self-similar variable, $\tilde{\Delta}(x)$ is the jet's half-width at the downstream distance x and y is the coordinate transversal to the jet's axis (see Fig. 13).

Defining \tilde{b}_u as the value of y where $\tilde{u} = \frac{1}{2}\tilde{u}_m$, the relationship between $\tilde{\Delta}$ and \tilde{b}_u is simply given by $\tilde{b}_u(x) = \text{ach}(\sqrt{2})\tilde{\Delta}(x)$.

The analytical solutions for the jet's centerline velocity and half-width are provided by Bickley (1937) as: $\tilde{u}_m(x) = \left(\frac{3M^2}{32\rho^2\nu x}\right)^{1/3}$ and $\tilde{\Delta}(x) = \left(\frac{48\rho\nu^2 x^2}{M}\right)^{1/3}$ respectively.

For the case of a 2D Poiseuille inlet flow, the constant momentum flux is $M = \int_{-\infty}^{+\infty} \rho\tilde{u}^2 dy = (6/5)\rho u_j^2 b$. Since the mass flux is assumed to be constant at any downstream location, the centerline velocity \tilde{u}_m can be expressed as:

$$\tilde{u}_m(x) = \frac{3}{10}u_j \left(\frac{5Re_j}{x/b}\right)^{1/3} \quad (17)$$

We note here that the analytical solution features a singular point at $x = 0$ due to the assumption that the jet flow begins at a narrow orifice of infinitesimal width (Bickley 1937; Schlichting 1960).

Consequently, and in order to fit with the experimental and simulated data, the equations need to be adjusted by introducing a virtual origin $\tilde{\lambda}$ (see Fig. 13), which has been estimated in previous works (Andrade and Tsien 1937; Andrade 1939; Revuelta et al. 2002). Revuelta and co-workers (2002) gave for instance a numerical estimation of $\tilde{\lambda}$ for both plane and round jets as a function of Re_j and b . The expression of $\tilde{\lambda}$ for a laminar plane free jet with Poiseuille injection reads: $\tilde{\lambda} = 0.029Re_j b$. After introducing the virtual origin, the centerline velocity and the jet's half-width become:

$$\tilde{u}_m(x) = \frac{3}{10}u_j \left(\frac{5Re_j}{(x + \tilde{\lambda})/b} \right)^{1/3} \quad (18)$$

$$\tilde{\Delta}(x) = 40^{1/3}bRe_j^{-2/3} \left(\frac{x + \tilde{\lambda}}{b} \right)^{2/3} \quad (19)$$

with x being now the downstream distance from the nozzle.

REFERENCES

- Andrade, E. N. D. C. (1939). "The velocity distribution in a liquid-into-liquid jet. part 2: the plane jet." *Proceedings of the Physical Society*, 51(5), 784.
- Andrade, E. N. D. C. and Tsien, L. C. (1937). "The velocity-distribution in a liquid-into-liquid jet." *Proceedings of the Physical Society*, 49(4), 381.
- Badr, S., Gauthier, G., and Gondret, P. (2014). "Erosion threshold of a liquid immersed granular bed by an impinging plane liquid jet." *Physics of Fluids*, 26(2), 023302.
- Beltaos, S. and Rajaratnam, N. (1973). "Plane turbulent impinging jets." *Journal of Hydraulic Research*, 11(1), 29–59.
- Beltaos, S. and Rajaratnam, N. (1974). "Impinging circular turbulent jets." *Journal of the hydraulics division*, 100(10), 1313–1328.
- Beltaos, S. and Rajaratnam, N. (1977). "Impingement of axisymmetric developing jets." *Journal of Hydraulic Research*, 15(4), 311–326.
- Bennett, S. J. and Alonso, C. V. (2005). "Kinematics of flow within headcut scour holes on hillslopes." *Water Resources Research*, 41(9).
- Bhatnagar, P. L., Gross, E. P., and Krook, M. (1954). "A model for collision processes in gases. i. small amplitude processes in charged and neutral one-component systems." *Phys. Rev.*, 94, 511–525.
- Bickley, W. (1937). "The plane jet." *The London, Edinburgh, and Dublin Philosophical Magazine and Journal of Science*, 23, 727–731.
- Bonelli, S. (2012). *Erosion of geomaterials*. Wiley-ISTE, New York.
- Bonelli, S. (2013). *Erosion in geomechanics applied to dams and levees*. Wiley-ISTE, New York.
- Boutt, D. F., Cook, B. K., McPherson, B. J., and Williams, J. (2007). "Direct simulation of fluid-solid mechanics in porous media using the discrete element and lattice-boltzmann methods." *Journal of Geophysical Research: Solid Earth*, 112(B10).
- Bouzidi, M., Firdaouss, M., and Lallemand, P. (2001). "Momentum transfer of a boltzmann-lattice fluid with boundaries." *Physics of Fluids*, 13(11), 3452–3459.

- Brunier-Coulin, F., Cuéllar, P., and Philippe, P. (2017a). “Erosion onset of a cohesionless granular medium by an immersed impinging round jet.” *Phys. Rev. Fluids*, 2, 034302.
- Brunier-Coulin, F., Sarrat, J.-L., Cuéllar, P., and Philippe, P. (2017b). “Experimental investigation of impinging jet erosion on model cohesive granular materials.” *8th International Conference on Micromechanics of Granular Media (Powders and Grains)*, Montpellier, France, EPJ Web of Conferences 140, 08002 (3-7 July).
- Chapman, S. and Cowling, T. G. (1970). *The mathematical theory of non-uniform gases: an account of the kinetic theory of viscosity, thermal conduction and diffusion in gases*. Cambridge university press.
- Chen, H., Chen, S., and Matthaeus, W. H. (1992). “Recovery of the navier-stokes equations using a lattice-gas boltzmann method.” *Phys. Rev. A*, 45, R5339–R5342.
- Chen, S., Martínez, D., and Mei, R. (1996). “On boundary conditions in lattice boltzmann methods.” *Physics of Fluids*, 8(9), 2527–2536.
- Cuéllar, P., Benseghier, Z., Luu, L.-H., Bonelli, S., Delenne, J.-Y., Radjaï, F., and Philippe, P. (2017). “Numerical insight into the micromechanics of jet erosion of a cohesive granular material.” *EPJ Web Conf.*, 140, 15017.
- Cuéllar, P., Philippe, P., Bonelli, S., Benahmed, N., Brunier-Coulin, F., Ngoma, J., Delenne, J.-Y., and Radjai, F. (2015). “Micromechanical analysis of the surface erosion of a cohesive soil by means of a coupled LBM-DEM model.” *IV International Conference on Particle-based Methods (PARTICLES 2015)*, 1121 p.
- Cui, X., Li, J., Chan, A., and Chapman, D. (2012). “A 2D DEM-LBM study on soil behaviour due to locally injected fluid.” *Particuology*, 10(2), 242–252.
- Cui, X., Li, J., Chan, A., and Chapman, D. (2014). “Coupled DEM-LBM simulation of internal fluidisation induced by a leaking pipe.” *Powder Technology*, 254, 299–306.
- Cundall, P. A. and Strack, O. D. L. (1979). “A discrete numerical model for granular assemblies.” *Géotechnique*, 29(1), 47–65.
- Feng, Y. T., Han, K., and Owen, D. R. (2007). “Coupled lattice Boltzmann method and dis-

crete element modelling of particle transport in turbulent fluid flows: Computational issues.”
International Journal for Numerical Methods in Engineering, 72(9), 1111–1134.

Foster, M., Fell, R., and Spannagle, M. (2000). “The statistics of embankment dam failures and accidents.” *Canadian Geotechnical Journal*, 37(5), 1000–1024.

Ghaneeizad, S. M., Atkinson, J. F., and Bennett, S. J. (2015). “Effect of flow confinement on the hydrodynamics of circular impinging jets: implications for erosion assessment.” *Environmental Fluid Mechanics*, 15(1), 1–25.

Gholamreza-Kashi, S., Martinuzzi, R. J., and Baddour, R. E. (2007). “Mean Flow Field of a Nonbuoyant Rectangular Surface Jet.” *Journal of Hydraulic Engineering*, 133(2), 234–239.

Guo, J. (1997). “Discussion of "the albert shields story" by junke guo.” *Journal of Hydraulic Engineering*, 123(7), 666–666.

Guo, J. (2002). “Hunter rouse and shields diagram.” *Advances in Hydraulics and Water Engineering: Volumes I & II*, World Scientific, 1096–1098.

Han, K., Feng, Y., and Owen, D. (2007). “Coupled lattice boltzmann and discrete element modelling of fluid-particle interaction problems.” *Computers & Structures*, 85(11), 1080–1088 Fourth MIT Conference on Computational Fluid and Solid Mechanics.

Han, Y. and Cundall, P. A. (2013). “LBM-DEM modeling of fluid-solid interaction in porous media.” *International Journal for Numerical and Analytical Methods in Geomechanics*, 37(10), 1391–1407.

Hanson, G. and Cook, K. (2004). “Apparatus, test procedures, and analytical methods to measure soil erodibility in situ.” *Applied engineering in agriculture*, 20(4), 455.

Hanson, G. J., Robinson, K. M., and Temple, D. M. (1990). “Pressure and stress distributions due to a submerged impinging jet.” *Hydraulic Engineering*, ASCE, 525–530.

Jambunathan, K., Lai, E., Moss, M. A., and Button, B. L. (1992). “A review of heat transfer data for single circular jet impingement.” *International Journal of Heat and Fluid Flow*.

Kuang, S., LaMarche, C., Curtis, J., and Yu, A. (2013). “Discrete particle simulation of jet-induced cratering of a granular bed.” *Powder Technology*, 239, 319–336.

- Ladd, A. J. C. (1994). “Numerical simulations of particulate suspensions via a discretized boltzmann equation. part 1. theoretical foundation.” *Journal of Fluid Mechanics*, 271, 285–309.
- Lallemand, P. and Luo, L.-S. (2000). “Theory of the lattice boltzmann method: Dispersion, dissipation, isotropy, galilean invariance, and stability.” *Phys. Rev. E*, 61, 6546–6562.
- Lallemand, P. and Luo, L.-S. (2003). “Lattice boltzmann method for moving boundaries.” *Journal of Computational Physics*, 184(2), 406–421.
- Latt, J. (2007). “How to implement your DdQq dynamics with only q variables per node (instead of 2q).” *Technical report*, Tufts University, Medford, USA.
- Latt, J., Chopard, B., Malaspinas, O., Deville, M., and Michler, A. (2008). “Straight velocity boundaries in the lattice boltzmann method.” *Phys. Rev. E*, 77, 056703.
- Lominé, F., Scholtes, L., Sibille, L., and Poullain, P. (2013). “Modeling of fluid–solid interaction in granular media with coupled lattice boltzmann/discrete element methods: application to piping erosion.” *International Journal for Numerical and Analytical Methods in Geomechanics*, 37(6), 577–596.
- Looney, M. K. and Walsh, J. J. (1984). “Mean-flow and turbulent characteristics of free and impinging jet flows.” *Journal of Fluid Mechanics*, 147(7), 397–429.
- Mansouri, M., El Youssoufi, M. S., and Nicot, F. (2016). “Numerical simulation of the quicksand phenomenon by a 3D coupled Discrete Element - Lattice Boltzmann hydromechanical model.” *International Journal for Numerical and Analytical Methods in Geomechanics*.
- Martin, H. (1977). “Heat and Mass Transfer between Impinging Gas Jets and Solid Surfaces.” *Advances in Heat Transfer*.
- Mattila, K., Hyväluoma, J., Rossi, T., Aspnäs, M., and Westerholm, J. (2007). “An efficient swap algorithm for the lattice boltzmann method.” *Computer Physics Communications*, 176(3), 200–210.
- Mei, R., Yu, D., Shyy, W., and Luo, L.-S. (2002). “Force evaluation in the lattice boltzmann method involving curved geometry.” *Phys. Rev. E*, 65, 041203.
- Mercier, F., Golay, F., Bonelli, S., Anselmet, F., Borghi, R., and Philippe, P. (2014). “2d axisymmet-

769 rical numerical modelling of the erosion of a cohesive soil by a submerged turbulent impinging
770 jet.” *European Journal of Mechanics - B/Fluids*, 45, 36–50.

771 Mutabaruka, P., Delenne, J.-Y., Soga, K., and Radjai, F. (2014). “Initiation of immersed granular
772 avalanches.” *Phys. Rev. E*, 89, 052203.

773 Ngoma, J., Philippe, P., Bonelli, S., Radjaï, F., and Delenne, J.-Y. (2018). “Two-dimensional
774 numerical simulation of chimney fluidization in a granular medium using a combination of
775 discrete element and lattice boltzmann methods.” *Phys. Rev. E*, 97, 052902.

776 Phares, D. J., Smedley, G. T., and Flagan, R. C. (2000). “The wall shear stress produced by the
777 normal impingement of a jet on a flat surface.” *Journal of Fluid Mechanics*, 418, 351–375.

778 Poreh, M., Tsuei, Y. G., and Cermak, J. E. (1967). “Investigation of a Turbulent Radial Wall Jet.”
779 *Journal of Applied Mechanics*.

780 Qian, Y. H., D’Humières, D., and Lallemand, P. (1992). “Lattice bgk models for navier-stokes
781 equation.” *EPL (Europhysics Letters)*, 17(6), 479.

782 Rajaratnam, N. (1976). “Turbulent jets.” *Developments in Water Science*.

783 Revuelta, A., Sanchez, A., and Linan, A. (2002). “The virtual origin as a first-order correction for
784 the far-field description of laminar jets.” *Physics of Fluids*, 14(6), 1821–1824.

785 Schlichting, H. (1960). *Boundary Layer Theory*. McGraw-Hill, 4th edition.

786 Shields, A. (1936). “Anwendung der Ähnlichkeitsmechanik und der Turbulenzforschung auf die
787 Geschiebebewegung.” *Preussische Versuchsanstalt für Wasserbau und Schiffbau*, Heft 26 (in
788 German), (English translation by W. P. Ott and J. C. van Uchelen available as *Hydrodynamics*
789 *Laboratory Publication No. 167*, Hydrodynamics Lab., California Inst. of Tech., Pasadena).

790 Streeter, V. L. and Wylie, E. B. (1975). *Fluid mechanics*. McGraw-Hill, New York, 6th edition.

791 Swope, W. C., Andersen, H. C., Berens, P. H., and Wilson, K. R. (1982). “A computer simulation
792 method for the calculation of equilibrium constants for the formation of physical clusters of
793 molecules: Application to small water clusters.” *The Journal of Chemical Physics*, 76(1), 637–
794 649.

795 Ting, J. M. and Corkum, B. T. (1992). “Computational laboratory for discrete element geomechan-

796 ics.” *Journal of computing in civil engineering*, 6(2), 129–146.

797 Yu, D., Mei, R., Luo, L.-S., and Shyy, W. (2003). “Viscous flow computations with the method of

798 lattice boltzmann equation.” *Progress in Aerospace Sciences*, 39(5), 329–367.

799 Zou, Q. and He, X. (1997). “On pressure and velocity boundary conditions for the lattice boltzmann

800 BGK model.” *Physics of Fluids*, 9(6), 1591–1598.

801

List of Tables

802

1 Input parameters used for the study cases with free jet configuration 35

803

2 Input parameters used for the study cases with impinging jet configuration 36

804

3 Input parameters for a parametric study of the erosion threshold 37

TABLE 1. Input parameters used for the study cases with free jet configuration

U_0 (m/s)	b (mm)	$\nu \times 10^{-6}$ (m ² /s)	Re_j (-)
0.37	5.2	33	38.9
0.37	5.2	66	19.4
0.185	10.8	16.5	80.7
0.185	5.2	16.5	38.9
0.185	10.8	33	40.4
0.185	5.2	33	19.4
0.74	5.2	33	77.7
0.37	10.8	33	80.7
0.37	6.8	33	50.8
0.37	8.4	33	62.8
0.37	12.4	33	92.7
0.62	5.2	16.5	130.3
0.53	5.2	16.5	111.4

TABLE 2. Input parameters used for the study cases with impinging jet configuration

Case	U_0 (m/s)	b (mm)	$\nu \times 10^{-6}$ (m ² /s)	Re_j (-)	H (mm)
a, b	0.37	5.2	33	38.9	90.4
a, b	0.74	5.2	33	77.7	90.4
a, b	0.5	5.2	33	52.5	90.4
a, b	0.6	5.2	33	63.03	90.4
a, b	0.37	6.8	33	50.8	90.4
a, b	0.74	6.8	33	101.7	90.4
a	0.37	5.2	33	38.9	73.2
a	0.74	5.2	33	77.7	73.2
a	0.37	6.8	33	50.8	73.2
a	0.37	5.2	33	38.9	108
a	0.74	5.2	33	77.7	108
a	0.37	6.8	33	50.8	108
a	0.74	5.2	10	256.5	90.4
a	0.37	5.2	10	128.3	90.4
a	0.74	5.2	100	25.7	90.4
a	0.37	5.2	100	12.8	90.4

TABLE 3. Input parameters for a parametric study of the erosion threshold

Solid particles	Fluid
Density ρ_s : 2230 kg/m^3	Density ρ_f : 847 kg/m^3
Normal stiffness k_n : 1.1×10^5	Kinematic viscosity ν :
Shear stiffness k_t : 1.1×10^5	$30 \text{ to } 50 \times 10^{-6} \text{ m}^2/\text{s}$
Friction coefficient μ : 0.3	Nozzle diameter b : 5.2 mm
Rolling friction μ_r : 0.1	Impingement height H : 90 mm
Restitution coefficient e : 0.2	
Gravitational acceleration g : 9.81 m/s^2	

List of Figures

- 1 Paradigm of free jet and impinging jet on a granular sample. The hydrodynamic variable $\tilde{u}_m(H)$ represents the free jet centerline velocity at a distance equal to the impingement height H , while V is the maximal fluid velocity over the impinged surface. 41
- 2 Sketch of study cases for jet analysis. Left: Free jet configuration; Right: Impinging jet on either a smooth wall (case a) or on a granular surface (case b) with distinction of the three characteristic jet flow regions. 42
- 3 Simulation results for a laminar 2D free jet with Poiseuille inlet ($U_0 = 0.37$ m/s, $b = 5.2 \times 10^{-3}$ m, $\nu = 33 \times 10^{-6}$ m²/s, and $Re_j = 38.9$). The curves represent the dimensionless centerline velocity u_m/U_0 along the dimensionless downstream distance x/b from the nozzle using the regularized (red circle line) and equilibrium (blue triangle line) boundary conditions for the inlet, as compared to the analytical solutions of the 2D laminar free jet using virtual origin given by (Revuelta et al. 2002) (dotted line) or by Eq. (9) (solid line), respectively. The dashed line represents the impinging jet on a smooth wall with $H = 90.4$ mm for the same inlet conditions. 43
- 4 Transversal profiles of fluid velocity for a laminar 2D free jet with Poiseuille inlet (same conditions as in Fig. 3). (a) Dimensionless fluid velocity u/U_0 versus dimensionless transversal coordinate y/b at different downstream distances x/b from the jet's nozzle. (b) Profiles of fluid velocity u normalized by the maximum (centerline) value u_m at each downstream location x/b ; the coordinate y is now normalized by b_u , the transversal distance where $u(b_u) = \frac{1}{2}u_m$ 44
- 5 (a) Variation of $(u_j/u_m)^3$ (●) and $(b_u/b)^{3/2}$ (○) with the normalized distance from the nozzle x/b for $Re_j = 38.9$; the solid lines are linear fits: $(u_j/u_m)^3 = \alpha(\frac{x+\lambda_u}{b})$ and $(b_u/b)^{3/2} = \beta(\frac{x+\lambda_b}{b})$ with $\alpha = 0.201$, $\beta = 0.138$, $\lambda_u/b = 1.29$, and $\lambda_b/b = 1.48$. (b) Log-log representation of the slopes α and β versus Re_j ; the lines represent the theoretical predictions extracted from Eqs. (18) and (19) in Appendix I. 45

832	6	Variation of the dimensionless virtual origin λ/b versus the jet Reynolds number	
833		Re_j obtained from the linear regression of the profiles $(u_j/u_m)^3$ (●) and $(b_u/b)^{3/2}$	
834		(○). The linear trend fitting the data is shown as a dashed line and the solid line is	
835		the expression of $\tilde{\lambda}$ provided by (Revuelta et al. 2002).	46
836	7	Profiles of transverse velocity v for different distances x_1 from the impingement	
837		surface, both for the smooth wall configuration (a) and for a fixed granular surface	
838		with mean grain size $d = 5$ mm (b) ($b/d = 1.04$ and $b_u/d = 1.93$ with b_u deduced	
839		from Eq. 19 with free jet model). The general simulation parameters are $H = 90.4$	
840		mm and $U_0 = 0.37$ m/s. For symmetry reason, only the right part of the transverse	
841		velocity profiles are shown for the smooth wall configuration.	47
842	8	Variation of maximum velocity V versus the free jet velocity $\tilde{u}_m(H + \lambda)$ at the	
843		corresponding downstream distance $x = H$ for a laminar jet impingement on either	
844		a smooth wall or on fixed granular surfaces with mean grain sizes $d = 3$ mm and 5	
845		mm respectively. The solid line is a linear fit from the smooth wall results.	48
846	9	(a) Transversal profiles of dimensionless wall shear stress for different combinations	
847		of normalized impingement height H/b and jet Reynolds number Re_j . The solid	
848		line represents the estimation provided by (Beltaos and Rajaratnam 1974). (b)	
849		Maximum shear stress τ_m on a smooth impinged surface versus $\rho V^2/\sqrt{Re_j}$	49
850	10	Time sequence of jet erosion on a frictional granular sample composed of 3000	
851		particles with $d_{mean} = 2$ mm, $\nu = 50 \times 10^{-6}$ m ² /s, $b = 5.2$ mm. A color scale	
852		is used for fluid velocity magnitude from zero (blue) to maximal inlet velocity U_0	
853		(red). Solid particles with kinetic energy above a critical threshold are classified as	
854		eroded (here depicted in red colour).	50

855	11	Critical values of inertial Shields number Sh_u^* versus particle Reynolds number	
856		Re_p^* for the simulated jet erosion of frictional granular beds, as compared to the	
857		experimental results of (Badr et al. 2014) (●). The simulations were performed	
858		with different values of mean particle size d and fluid kinematic viscosity ν : $d = 2$	
859		mm (▲), $d = 3$ mm (○), and $d = 5$ mm (□) with $\nu = 4 \times 10^{-5} \text{ m}^2\text{s}^{-1}$; $d = 2$ mm	
860		(△), $d = 3$ mm (●), and $d = 5$ mm (■) with $\nu = 5 \times 10^{-5} \text{ m}^2\text{s}^{-1}$; $d = 2$ mm (▽)	
861		with $\nu = 3.3 \times 10^{-5} \text{ m}^2\text{s}^{-1}$; $d = 3$ mm (▼) with $\nu = 3.75 \times 10^{-5} \text{ m}^2\text{s}^{-1}$; $d = 5$ mm	
862		(◆) with $\nu = 3 \times 10^{-5} \text{ m}^2\text{s}^{-1}$; $d = 5$ mm (◇) with $\nu = 3.7 \times 10^{-5} \text{ m}^2\text{s}^{-1}$	51
863	12	Critical Shields number Sh_τ^* versus particle Reynolds number Re_τ^* at the threshold.	
864		The solid line stands for the explicit Shields equation [Eq. (14)]. The symbols are	
865		the same as those used in Fig. 11.	52
866	13	Sketch of a plane free jet with virtual origin λ located above the nozzle exit.	53

Fig1.pdf

Fig. 1. Paradigm of free jet and impinging jet on a granular sample. The hydrodynamic variable $\tilde{u}_m(H)$ represents the free jet centerline velocity at a distance equal to the impingement height H , while V is the maximal fluid velocity over the impinged surface.

Fig2.pdf

Fig. 2. Sketch of study cases for jet analysis. Left: Free jet configuration; Right: Impinging jet on either a smooth wall (case a) or on a granular surface (case b) with distinction of the three characteristic jet flow regions.

Fig. 3. Simulation results for a laminar 2D free jet with Poiseuille inlet ($U_0 = 0.37$ m/s, $b = 5.2 \times 10^{-3}$ m, $\nu = 33 \times 10^{-6}$ m²/s, and $Re_j = 38.9$). The curves represent the dimensionless centerline velocity u_m/U_0 along the dimensionless downstream distance x/b from the nozzle using the regularized (red circle line) and equilibrium (blue triangle line) boundary conditions for the inlet, as compared to the analytical solutions of the 2D laminar free jet using virtual origin given by (Revuelta et al. 2002) (dotted line) or by Eq. (9) (solid line), respectively. The dashed line represents the impinging jet on a smooth wall with $H = 90.4$ mm for the same inlet conditions.

Fig4a.eps

(a)

Fig4b.eps

(b)

Fig. 4. Transversal profiles of fluid velocity for a laminar 2D free jet with Poiseuille inlet (same conditions as in Fig. 3). (a) Dimensionless fluid velocity u/U_0 versus dimensionless transversal coordinate y/b at different downstream distances x/b from the jet's nozzle. (b) Profiles of fluid velocity u normalized by the maximum (centerline) value u_m at each downstream location x/b ; the coordinate y is now normalized by b_u , the transversal distance where $u(b_u) = \frac{1}{2}u_m$.

Fig5a.eps

(a)

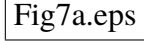
Fig5b.eps

(b)

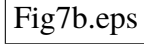
Fig. 5. (a) Variation of $(u_j/u_m)^3$ (●) and $(b_u/b)^{3/2}$ (○) with the normalized distance from the nozzle x/b for $Re_j = 38.9$; the solid lines are linear fits: $(u_j/u_m)^3 = \alpha(\frac{x+\lambda_u}{b})$ and $(b_u/b)^{3/2} = \beta(\frac{x+\lambda_b}{b})$ with $\alpha = 0.201$, $\beta = 0.138$, $\lambda_u/b = 1.29$, and $\lambda_b/b = 1.48$. (b) Log-log representation of the slopes α and β versus Re_j ; the lines represent the theoretical predictions extracted from Eqs. (18) and (19) in Appendix I.

Fig6.eps

Fig. 6. Variation of the dimensionless virtual origin λ/b versus the jet Reynolds number Re_j obtained from the linear regression of the profiles $(u_j/u_m)^3$ (●) and $(b_u/b)^{3/2}$ (○). The linear trend fitting the data is shown as a dashed line and the solid line is the expression of $\tilde{\lambda}$ provided by (Revuelta et al. 2002).

Fig7a.eps

(a) Smooth wall

Fig7b.eps

(b) Granular surface

Fig. 7. Profiles of transverse velocity v for different distances x_1 from the impingement surface, both for the smooth wall configuration (a) and for a fixed granular surface with mean grain size $d = 5$ mm (b) ($b/d = 1.04$ and $b_u/d = 1.93$ with b_u deduced from Eq. 19 with free jet model). The general simulation parameters are $H = 90.4$ mm and $U_0 = 0.37$ m/s. For symmetry reason, only the right part of the transverse velocity profiles are shown for the smooth wall configuration.

Fig8.eps

Fig. 8. Variation of maximum velocity V versus the free jet velocity $\tilde{u}_m(H + \lambda)$ at the corresponding downstream distance $x = H$ for a laminar jet impingement on either a smooth wall or on fixed granular surfaces with mean grain sizes $d = 3$ mm and 5 mm respectively. The solid line is a linear fit from the smooth wall results.

Fig9a.eps

(a)

Fig9b.eps

(b)

Fig. 9. (a) Transversal profiles of dimensionless wall shear stress for different combinations of normalized impingement height H/b and jet Reynolds number Re_j . The solid line represents the estimation provided by (Beltaos and Rajaratnam 1974). (b) Maximum shear stress τ_m on a smooth impinged surface versus $\rho V^2 / \sqrt{Re_j}$.

Fig10a.pdf

(a) $t = 12.5$ s, $Re_j = 40.21$, $U_0 = 0.58$ m/s

Fig10b.pdf

(b) $t = 15$ s, $Re_j = 45.76$, $U_0 = 0.66$ m/s

Fig10c.pdf

(c) $t = 17.5$ s, $Re_j = 50$, $U_0 = 0.72$ m/s

Fig10d.pdf

(d) $t = 20$ s, $Re_j = 55.47$, $U_0 = 0.8$ m/s

Fig10e.pdf

(e) $t = 22.5$ s, $Re_j = 61.01$, $U_0 = 0.88$ m/s

Fig10f.pdf

(f) $t = 25$ s, $Re_j = 69.33$, $U_0 = 1$ m/s

Fig. 10. Time sequence of jet erosion on a frictional granular sample composed of 3000 particles with $d_{mean} = 2$ mm, $\nu = 50 \times 10^{-6}$ m²/s, $b = 5.2$ mm. A color scale is used for fluid velocity magnitude from zero (blue) to maximal inlet velocity U_0 (red). Solid particles with kinetic energy above a critical threshold are classified as eroded (here depicted in red colour).

Fig. 11. Critical values of inertial Shields number Sh_u^* versus particle Reynolds number Re_p^* for the simulated jet erosion of frictional granular beds, as compared to the experimental results of (Badr et al. 2014) (●). The simulations were performed with different values of mean particle size d and fluid kinematic viscosity ν : $d = 2$ mm (▲), $d = 3$ mm (○), and $d = 5$ mm (□) with $\nu = 4 \times 10^{-5}$ m²s⁻¹; $d = 2$ mm (△), $d = 3$ mm (●), and $d = 5$ mm (■) with $\nu = 5 \times 10^{-5}$ m²s⁻¹; $d = 2$ mm (▽) with $\nu = 3.3 \times 10^{-5}$ m²s⁻¹; $d = 3$ mm (▼) with $\nu = 3.75 \times 10^{-5}$ m²s⁻¹; $d = 5$ mm (◆) with $\nu = 3 \times 10^{-5}$ m²s⁻¹; $d = 5$ mm (◇) with $\nu = 3.7 \times 10^{-5}$ m²s⁻¹.

Fig12.eps

Fig. 12. Critical Shields number Sh_τ^* versus particle Reynolds number Re_τ^* at the threshold. The solid line stands for the explicit Shields equation [Eq. (14)]. The symbols are the same as those used in Fig. 11.

Fig13.pdf

Fig. 13. Sketch of a plane free jet with virtual origin λ located above the nozzle exit.